УДК 556.55:532.542.4

© *С. Р. Богданов*[1], *Р. Э. Здоровеннов*[1], *Н. И. Пальшин*[1], *Г. Э. Здоровеннова*[1]*, *А. Ю. Тержевик*[1], *Г. Г. Гавриленко*[1], *С. Ю. Волков*[1], *Т. В. Ефремова*[1], *Н. А. Кулдин*[2], *Г. Б. Кириллин*[3]

© Перевод: *Е. С. Кочеткова*, 2021

[1]Институт водных проблем Севера КарНЦ РАН, 185030, пр. Александра Невского, д. 50, г. Петрозаводск, Россия
[2]Петрозаводский государственный университет, 185910, пр. Ленина, д. 33, г. Петрозаводск, Россия
[3]Лейбниц-Институт пресноводной экологии и рыболовства внутренних водоемов, 12587 Мюггельзеедамм, 310, г. Берлин, Германия
*E-mail: zdorovennova@gmail.com

РАСЧЕТ ТУРБУЛЕНТНЫХ НАПРЯЖЕНИЙ В КОНВЕКТИВНО-ПЕРЕМЕШАННОМ СЛОЕ В МЕЛКОВОДНОМ ОЗЕРЕ ПОДО ЛЬДОМ С ИСПОЛЬЗОВАНИЕМ ДВУХ ADCP

Статья поступила в редакцию 28.07.2020, после доработки 21.09.2020

Представлен метод расчета турбулентных напряжений, основанный на использовании пары трехлучевых акустических допплеровских профилографов скорости, с одной или двумя точками пересечения лучей. Для апробации метода был спланирован и проведен специальный натурный эксперимент по измерению температуры воды, уровня подледной облученности и компонент скорости в конвективно-перемешанном слое покрытого льдом небольшого бореального озера. Полученные данные позволяют рассчитать не только интенсивности пульсаций вдоль трех ортогональных осей, но и недиагональные компоненты тензора Рейнольдса. С использованием условия однородности средней скорости по горизонтали получены количественные результаты, описывающие энергетику процессов в период весенней подледной конвекции: рассчитана анизотропия турбулентных пульсаций, изучена корреляция энергии турбулентности с интенсивностью накачки (через поток плавучести). Приведен качественный анализ параметров и динамики энергосодержащих структур, развивающихся в конвективном слое небольших покрытых льдом озер весной.

Ключевые слова: бореальное озеро, температура воды, подледная радиация, поток плавучести, скорости течений, конвективно-перемешанный слой, акустические допплеровские профилографы, тензор турбулентных напряжений, анизотропия турбулентных пульсаций.

© *S. R. Bogdanov*[1], *R. E. Zdorovennov*[1], *N. I. Palshin*[1], *G. E. Zdorovennova*[1]*, *A. Yu. Terzhevik*[1], *G. G. Gavrilenko*[1], *S. Yu. Volkov*[1], *T. V. Efremova*[1], *N. A. Kuldin*[2], *G. B. Kirillin*[3]

© Translation: *E. S. Kochetkova*, 2021

[1]Northern Water Problems Institute Karelian Research Center of RAS,
185030, Aleksandra Nevskogo Pr., 50, Petrozavodsk, Russia
[2]Petrozavodsk State University, 185910, Lenina Pr., 33, Petrozavodsk, Russia
[3]Department of Ecohydrology, Leibniz-Institute of Freshwater Ecology and Inland Fisheries (IGB),
12587, Müggelseedamm, 310, Berlin, Germany
*E-mail: zdorovennova@gmail.com

DERIVING OF TURBULENT STRESSES IN A CONVECTIVELY MIXED LAYER IN A SHALLOW LAKE UNDER ICE BY COUPLING TWO ADCPS

Received 28.07.2020, in final form 21.09.2020

This paper presents a method for deriving turbulent stresses using a pair of ADCPs with one or two points of beam intersections. A specific experiment, which includes measurements of water temperature, under-ice irradiation levels, and velocity components in the convectively mixed layer of a shallow ice-covered boreal lake, validated the method. The experimental data allows calculations of both the pulsation intensities along the three orthogonal axes and off-diagonal components of the Reynolds tensor. The specific features of spring under-ice convection processes, in particular, the anisotropy of turbulent pulsations and the

---

Ссылка для цитирования: *Богданов С.Р.*, *Здоровеннов Р.Э.*, *Пальшин Н.И.*, *Здоровеннова Г.Э.*, *Тержевик А.Ю.*, *Гавриленко Г.Г.*, *Волков С.Ю.*, *Ефремова Т.В.*, *Кулдин Н.А.*, *Кириллин Г.Б.* Расчет турбулентных напряжений в конвективно-перемешанном слое в мелководном озере подо льдом с использованием двух ADCP // Фундаментальная и прикладная гидрофизика. 2021. Т. 14, № 2. С. 17–28. doi: 10.7868/S2073667321020027

For citation: *Bogdanov S.R.*, *Zdorovennov R.E.*, *Palshin N.I.*, *Zdorovennova G.E.*, *Terzhevik A.Yu.*, *Gavrilenko G.G.*, *Volkov S.Yu.*, *Efremova T.V.*, *Kuldin N.A.*, *Kirillin G.B.* Deriving of Turbulent Stresses in a Convectively Mixed Layer in a Shallow Lake Under Ice by Coupling Two ADCPs. *Fundamentalnaya i Prikladnaya Gidrofizika*. 2021, 14, 2, 17–28. doi: 10.7868/S2073667321020027

correlation of turbulence energy with the turbulence energy production (as the buoyancy flux), were described using the horizontal homogeneity assumption. Finally, the paper presents a qualitative analysis of the parameters and dynamics of energy-containing structures developing in the convective layer of small ice-covered lakes in spring.

Key words: boreal lake, water temperature, under-ice radiation, buoyancy flux, current velocities, convectively mixed layer, acoustic Doppler profilers, turbulent stress tensor, anisotropy of turbulent pulsations.

1. Introduction

During the last three decades, acoustic Doppler profilers (ADCP) have been actively used in the study of water bodies [1—3]. Their principle of operation is based on measurements of the Doppler frequency shift between a pulsed ultrasonic signal and its reflection, or the phase shift between two successive pulses.

In the experiment, a popular ADCP version was used, in which short ultrasonic pulses are symmetrically diverged by three narrow beams at an angle α_0 =25° from the vertical. The velocity projections on the beams' directions b_i are measured directly at the points located on the beams. Velocity along each beam can be measured with the widely varying vertical resolution from centimeters to meters. In this case, neglecting the horizontal inhomogeneity of the flow, the average velocity for each layer, and the average velocity vertical profile can be estimated directly from the three registered "beam" components.

Along with the average speed estimation, when the condition of horizontal homogeneity is met, the device readings can serve as a basis for calculating some parameters of turbulence [4—6]. The corresponding tasks include the study of the small-scale structure of the velocity field with estimates of the energy dissipation rate ε based on the analysis of the quadratic structure functions of the velocity field [5] or spectra in the inertial interval [6]. The parameters of large-scale disturbances and the corresponding terms in the turbulent energy balance equation are also investigated. In this case, the main object of study are components $\rho\langle u_i'u_j'\rangle$ of the Reynolds tensor of turbulent stresses (unless otherwise stated, this term is used for the "kinematic version" of $\langle u_i'u_j'\rangle$ of this tensor), where ρ is the fluid density, and u_i', u_j' are the pulsating velocity components in the orthogonal coordinate system. To calculate the off-diagonal tensor components that determine the energy pumping and energy redistribution between the components in shear flows, usually, 4- or 5-beam devices are used [2, 6]. In the case of a symmetric arrangement of the beams relative to the vertical, for two such components, explicit expressions can be obtained in terms of the beam components' pulsations squares [7, 8].

For a complete analysis of the turbulent energy balance and the study of energy-containing structures configuration and topology in the convective layer, in the general case, all six components of the Reynolds tensor and, accordingly, three of its invariants are required. However, calculating these from the radial velocity components measured with 3-beam ADCPs remains to be solved. In this paper, we propose a solution to this problem, using two rigidly connected 3-beam ADCPs. The implementation of the method was carried out based on experimental data obtained in the study of spring under-ice convection in a shallow boreal lake. Convective motions in lakes under ice arise due to inhomogeneous heating of the water column, which leads to the appearance of a negative buoyancy flux [9]. On small lakes, the phenomenon of under-ice convection is usually observed at the end of the winter period [10], when, after the snow melts, there is a sharp increase in the radiation flux penetrating the ice.

In ice-covered lakes, along with convective mixing, various hydrodynamic processes are observed, such as advective transport, seiches, internal waves, eddies, density circulation caused by heat exchange of water mass with bottom sediments, as well as the atmospheric impact on the ice cover [11, 12]. These processes form a wide range of water temperature variability, level fluctuations, and current velocities in ice-covered lakes [13—16].

2. Research object and description of the experiment

The measurements were carried out between March 27—April 6, 2020, in small ice-covered shallow Lake Vendyurskoe, a reservoir of water-glacial origin typical for Fennoscandia. The lake's surface area is 10.4 km^2, the average depth is 5.3 m, and the maximum depth is 13.4 m. The ice-covered period lasts from November to May, the maximum ice thickness in different years reaches 0.4—0.8 m [17].

According to measurements on the Lake Vendyurskoe in March-April 1994—2019 (see, for example, [17]), the phenomenon of under-ice convection is observed annually. Under-ice convection usually begins in late March-early April and lasts 2—6 weeks. The under-ice gradient layer, the convectively mixed layer (CML), and the underlying stratified layer are the three layers that are clearly distinguished during developed convection on the vertical temperature profile. As the under-ice irradiation increases, the convection intensity increases, while the lower boundary of the CML deepens, and the CML temperature rises. Usually, by the time the ice breaks, the CML temperature reaches 3.5—4.5 °C, and its lower boundary deepens to 7—9 m.

Integrated measurements in the spring of 2020 included spatial ice and temperature surveys on March 29 at cross-section stations and multi-day measurements at autonomous stations between March 27 and April 6, 2020 (fig. 1, see Inset). Vertical soundings of temperature were carried out using a CTD-90M (temperature measurement accuracy ± 0.005 ºC, resolution 0.001 °C).

The measuring complex was located on the ice of the lake near the northern shore in an area with a depth of ~7 m (fig. 1, *a*) and included a radiation station (three "Star-shaped pyranometers" "Theodor Friderich & Co, Meteorologishe Gerate und Systeme", accuracy 0.2 W/m^2, one-minute time resolution), a thermistor chain with 13 temperature sensors (RBR Ltd., accuracy ± 0.002 °C, measurement interval 10 seconds) and two ADCPs (2 MHz HR Aquadopp current velocity profiler, Nortek AS, Norway) (fig. 1, *b*). The sensors were fixed on thermistor chain at depths from 0.2 to 6.2 m with an offset of 0.5 m. Using the thermistor chain data, the variability of the position of the CML lower boundary (h_{CML}) was studied in the period March 27 —April 6, 2020, which was determined as a depth of the isotherm with a value exceeding the average temperature of the CML by 0.05 °C. The depth of the under-ice stratified layer lower boundary δ was estimated with temperature data at the stations of the cross-section (fig. 1, *a*).

The two ADCPs were mounted on a special retaining frame that rigidly fixed the instruments on the ice and to each other. Both devices were installed in a hole with emitters located 3 cm below the lower ice boundary (fig. 2, *a*, see Inset). For the entire measurement period, the devices were set up as follows: signal discreteness was one minute (32 pulses with a frequency of 2 Hz), depth scanning range was 2.875 m (115 cells with a size of 25 mm). To exclude the mutual influence of the two ADCPs, the emitters were set in an asynchronous mode with a 30 s delay (fig. 2, *b*). Then the radial velocities were averaged over 16-s active series; further processing was carried out using these averages, for which the designations b_i. The root-mean-square error of b_i values varied in the range (0.1—0.5) mm/s.

The X-axes of both devices were oppositely directed (fig. 1, *b*). The measurements were carried out with two different versions of the mutual position of the devices: in the first experiment (Single crossing, SC), beams 1 and 4 intersected at point *C* at a depth $h = l_1/(2\ \mathrm{tg}\ \alpha_0)$, where the distance l_1 between the emitters *O* and *O*' was 1.5 m. In the second experiment (Double crossing, DC), there were two intersection points (beams 3 and 5, and 2 and 6 intersected, fig. 1, *b*), and the distance l_2 (0.75 m) between the emitters *O* and *O*′ was chosen as ($l_2 = l_1/2$), to ensure that in both experiments the beam intersections appear at the same depth *h*. At the depth corresponding to the intersection point of the beams, in the SC version, the beam components were measured at five points (*A*, *B*, *C*, *D*, *E* in fig. 1, *b*), and in the DC version, at four (points *E*, *F*, *G*, *H* in fig. 1, *b*). The SC setting of the devices was used from 17:00 on March 27 to 9:30 on March 30, and the DC experiment was conducted between 10:00, March 30, and 10:00, April 6, 2020.

3. Method for calculating turbulent stresses with data from two ADCPs

Choosing the orthogonal *XYZ* system associated with the first device (fig. 1, *b*), the radial velocity components after simple trigonometric calculations can be directly expressed in terms of the orthogonal velocity components (u_x, u_y, u_z) at the corresponding point. For example, for SC configuration:

$$\begin{cases} b_1 = u_x(C)\sin\alpha_0 + u_z(C)\cos\alpha_0; \\ b_2 = -u_x(B)\frac{1}{2}\sin\alpha_0 + u_y(B)\frac{\sqrt{3}}{2}\sin\alpha_0 + u_z(B)\cos\alpha_0; \\ b_3 = -u_x(A)\frac{1}{2}\sin\alpha_0 - u_y(A)\frac{\sqrt{3}}{2}\sin\alpha_0 + u_z(A)\cos\alpha_0; \end{cases} \tag{1}$$

$$\begin{cases} b_4 = -u_x(C)\sin\alpha_0 + u_z(C)\cos\alpha_0; \\ b_5 = u_x(D)\frac{1}{2}\sin\alpha_0 - u_y(D)\frac{\sqrt{3}}{2}\sin\alpha_0 + u_z(D)\cos\alpha_0; \\ b_6 = u_x(E)\frac{1}{2}\sin\alpha_0 + u_y(E)\frac{\sqrt{3}}{2}\sin\alpha_0 + u_z(E)\cos\alpha_0. \end{cases}$$

In the general case, the right-hand sides of the above equations include 15 unknowns, i.e., the velocity components at points *A*, *B*, *C*, *D*, *E*, and six equations are not enough to determine them. However, the given system of equations becomes efficient in the case, which is quite widespread in the study of geophysical flows, when the flow can be considered locally homogeneous in the horizontal plane. For such cases, points *A*, *B*, *C*, *D*, and *E* can be considered quite close, meaning that the distance between them is significantly less than the horizontal scale characterizing the change in the mean flow. In this case, the components of the average velocity at different points can be considered the same, for example, $<u_x(A)>=<u_x(B)>=<u_x(C)>=<u_x(D)>=<u_x(E)>=U_x$, and the only three components of the average velocity (U_x, U_y, U_z) remain unknown. From now on, angle brackets denote time-averaged quantities.

System (1), due to linearity, retains its form for averaged values, so that three components of the average velocity in the *XYZ* system are calculated using any three equations of system (1) written for the average values $<b_i>$ of the beam components, for example:

$$\begin{pmatrix} <b_1> \\ <b_2> \\ <b_3> \end{pmatrix} = \sin\alpha_0 \begin{pmatrix} 1 & 0 & ctg\alpha_0 \\ -1/2 & \sqrt{3}/2 & ctg\alpha_0 \\ -1/2 & -\sqrt{3}/2 & ctg\alpha_0 \end{pmatrix} \begin{pmatrix} U_x \\ U_y \\ U_z \end{pmatrix}. \tag{2}$$

The matrix A on the right-hand side of eq. (2) is uniquely determined by the instrumental angle α_0. The inverse matrix $T=A^{-1}$, called transformation matrix, allows, following (2), direct calculation of the components (U_x, U_y, U_z) of the average velocity from the calculated average values $<b_i>$ of the beam components.

Similarly, the condition of local horizontal homogeneity allows calculation of the Reynolds stresses from directly calculated pulsation intensities $b_i' = b_i - <b_i>$ of the beam components. Note that the relationships (1) connecting the radial velocities b_i with the orthogonal components of the pulsation velocity at the corresponding point are linear.

As a consequence, representation (2) and similar to it for beams 4–6 remain valid for the corresponding pulsation components b_i'. Taking this into account, each of the $b_i'^2$ quantities can be directly expressed through the components of the stress tensor at the corresponding point, for example:

$$<b_1'^2> = <u_x'^2> \sin^2\alpha_0 + <u_z'^2> \cos^2\alpha_0 + 2<u_x' u_z'> \cos\alpha_0 \sin\alpha_0. \tag{3}$$

Here, the velocity pulsation components in the orthogonal coordinate system are denoted by the u' with the corresponding indices.

Under the assumption of local homogeneity in the horizontal plane, the statistical characteristics of the pulsation velocities at points located at the same depth are identical, for example $<u_x'^2(A)> = <u_x'^2(B)> = <u_x'^2(C)> \equiv <u_x'^2>$. In this case, using one 3-beam instrument, we obtain three equations of the form (3) for six unknowns. However, although the relationship between the squares of the beam pulsations and the components of the Reynolds tensor is linear, it is not possible to obtain explicit expressions for at least three diagonal components of the tensor (for the intensity of the pulsations along the orthogonal axes). From the results of measurements, it is possible to determine only some of their linear combinations.

In particular, equations of the form (3) do not allow calculating the intensities of pulsations along the orthogonal axes, or the total turbulent intensity $<u'^2>$. So, when summing up the intensities of "beam" pulsations, we obtain the expression,

$$<b_1'^2> + <b_2'^2> + <b_3'^2> = \frac{3}{2}\left(<u_x'^2> + <u_y'^2>\right)\sin^2\alpha_0 + 3<u_z'^2>\cos^2\alpha_0, \tag{4}$$

which contains no off-diagonal Reynolds components, and the horizontal and vertical pulsations are separated. Nevertheless, the intensity of turbulence u'^2 cannot be determined from this expression since the ratio of vertical pulsations to the total intensity $\zeta = <u_z'^2> / <u'^2>$ is unknown.

With a single 3-beam device, the problem can be partially solved only in some specific cases. For example, due to the modified configuration of the beams [18], it is possible to calculate the intensity of vertical pulsations, which is of particular interest for assessing vertical diffusion.

The use of 4-beam devices partly solves the problem. In this case, there are four equations of type (3), and, as noted in the introduction, with a symmetric arrangement of the beams, the cross components $<u_x'u_z'>$ and $<u_y'u_z'>$, which determine the pump intensity in shear flows, can be directly calculated from the difference of the squares of the pulsations of the corresponding beam components [1, 8].

For a complete solution, it is necessary to increase the number of independent equations of the type (3) to six. For this purpose, we used two coupled devices with a total number of beams of 6, which makes it possible to obtain six equations for the components of the Reynolds tensor.

The use of this equation system still does not lead to a complete solution to the problem. The determinant of the coefficient matrix of this system vanishes, which indicates its singularity. In other words, not all equations of the system are linearly independent. It is due to the azimuthally symmetric configuration of the beams of both devices. In this case, the sum of the beam intensities, of the first device, for instance, is determined by the formula (4) and does not depend on the horizontal orientation of the beams. A similar expression is valid for the second device, i.e., the sum of the first three equations of the system coincides with the sum of the last three, and one equation is not enough to find the six unknowns.

However, the problem can be solved with the chosen setting of the instruments, taking into account that two radial velocity components are simultaneously measured at the points of intersection. The averaged correlations of these components, for example, $<b_1'b_4'>$ in the SC setting using the matrix A (see (eq. 2)), can be represented as a linear combination of the orthogonal turbulent stresses:

$$< b_1'b_4' > = -< u_x'^2 > \sin^2 \alpha_0 + < u_z'^2 > \cos^2 \alpha_0 . \tag{5}$$

Equation (5) plays the role of a missing linearly independent equation. Moreover, there are two such equations in the DC setting (for correlations $<b_2'b_6'>$ and $<b_3'b_5'>$), so one of them can be used to verify the calculation results.

The noted specificity of the equation system also determines some of the features of data processing and calculation. Namely, with both settings of instruments, there are possible alternatives in the use of experimental data and, accordingly, in the choice of six independent equations. In this case, for example, for the first setting, two options are possible:

1. Exclude one of the equations for the beam intensities, replacing it with equation (5) for the correlation of the beam velocity pulsations at the intersection point. The advantages of this option include a reduction in the size of the horizontal spot, in which uniformity of parameters is assumed. However, there are two drawbacks, specifically, information on the intensity of pulsations along the direction of the excluded beam is not used and, additionally, (if any of beams 2, 3, 5, 6 are excluded), an artificially created asymmetry of the averaging region.

2. Use linear combinations of beam intensities. Here, with proper selection, both the symmetry of the spot and most of the information obtained are preserved. For example, one of the alternatives is that the system of equations uses their sum and equation (5) instead of the first (for $<b_1'^2>$) and fourth (for $<b_4'^2>$) equations. Apparently, there are numerous alternatives, especially in the DC setting.

In this work, the second option was used for the implementation of the method. The procedure for selecting independent equations and their specific form is presented in the Appendix.

The choice of the time averaging scale T is important in data processing and calculations. In the course of calculations, this scale was varied, and the characteristic time τ (turnover time) of relaxation of the energy-containing structures of the mixed layer was used as the minimum value of T [15]. The value of τ was calculated based on estimates of the characteristic size l_c integral scale of turbulence) and the velocity w_c pulsations in the energy-containing interval. For the value of l_c, the thickness of the convective layer [19] $h_C = (h_{CML}\text{-}\delta)$ was used as a governing parameter.

The characteristic scale of velocity pulsation w_c was identified with the so-called convective velocity w*, determined from the negative buoyancy B_R [19]: $w^* = (B_R h_C)^{1/3}$. In the case when gravitational instability is created due to the volumetric absorption of solar radiation $H(z)$ (W/m^2), B_R, which characterizes the pumping of convective energy in a vertically homogeneous layer h_C, is determined by the equation [10]:

$$B_R = \beta\left[I(\delta) + I(h_{CML}) - \frac{2}{h_c}\int_{\delta}^{h_{CML}} I(z)dz \right], \tag{6}$$

where $I = H/(c_p\rho)$ is a kinematic flow of solar radiation (K m/s), $\beta = \alpha_T g$ is a buoyancy coefficient, α_T is a coefficient of thermal expansion; ρ and c_p are density and specific heat of water at constant pressure.

The dependence of the flux I on the depth was approximated by an exponential with the extinction coefficient γ constant over the spectrum, time and depth, $I(z) = I(\delta)e^{-\gamma z}$. In this case, the expression for B_R assumes the form:

$$B_R = \beta I(\delta)\left[1 + \exp(-\gamma h_c) - \frac{2}{\gamma h_c}(1 - \exp(-\gamma h_c)) \right]. \tag{7}$$

The calculations of B_R and w* used $\gamma \approx 1{,}0$ м$^{-1}$ [16].

4. Results

4.1. Meteorological conditions, ice cover, solar radiation, temperature profile

During the period of the spatial survey on March 29, 2020, at the stations of the longitudinal and cross-sections, the total ice thickness varied within 35–49 cm, with an average value of 40 cm. At the station of the experimental complex, the total ice thickness was 40 cm, crystalline ice was 29 cm, and white ice thickness was 11 cm. In the period between March 29 and April 6, no active ice melting was observed. Fresh snow fell on April 1–2. The snow thickness at the time of measurements on April 6 was 1–2 cm.

In the period between March 28 and April 6, the daytime maximums of the incident radiation reached 600–800 W/m^2. In the first days of measurements on March 28–31, the ice surface was practically free of snow, and the daytime maximums of reflected radiation fluxes were 200–230 W/m^2, under ice — 90–100 W/m^2 (fig. 3, *a*, see Inset). After fresh snow fell on April 1–2, the daytime maximums of the reflected radiation flux increased sharply to 500–700 W/m^2, and under the ice, the radiation flux decreased to almost zero. On April 3–6, the fluxes of reflected radiation reached 300–500 W/m^2, and under ice, the radiation flux increased to 50–60 W/m^2.

During the measurement period on March 29, 2020, at the cross-section stations, the lower boundary of the underglacial stratified layer was at depths of 0.4–0.5 m. In the period between March 30 and April 1, the lower boundary of the CML actively deepened from 4.0 m to 5.5 m (fig. 3, *b*). After snowfall on April 1–2, the process of the convective layer deepening stopped, and on April 3–6 h_{CML} varied within 4–5 m. Thus, the SC setting between March 27–30 coincided with the active development of convection. For the DC setting, the convection phases changed from active development of convection (March 30–31) to its almost complete attenuation (April 1–2) and weak renewal (April 3–6). The evolution of temperature profiles is shown in fig. 3, *c*. The ADCP scanning area was within the CML for the entire measurement period (fig. 3, *b*).

The thickness of the convective layer h_C and with equation 7, the convective velocity w^* were calculated using estimates of h_{CML} and δ. The daily maximums of w^* varied in the range of 0.9–2.7 mm/s. For the relaxation time of energy-containing structures $\tau = h_c / w^*$ a lower estimate was obtained. Its value varied in the range 30–50 minutes. The latter estimate was further used as the basis for calculating the mean values. A 100 minutes interval was used as the time averaging base scale T.

4.2. Average velocity

The advantage of using two rigidly coupled ADCP instruments is the ability to check the horizontal uniformity condition for average speed directly. Fig. 4 shows (see Inset) the dependence of the horizontal components U_x and U_y on time, calculated separately for each instrument over the entire time interval of measurements for a depth of $h = 1.61$ m.

The results indicate that in the SC setting ($l_1 = 1.5$ м), sometimes the deviations from homogeneity were significant, especially for the Y velocity component. During the experiment in the DC setting, when the distance l_2 between the emitters was 0.75 m, the condition was fulfilled with a sufficiently high degree of accuracy.

4.3. Turbulent stresses

All six components of the turbulent stress tensor were calculated using directly derived values of the beam intensities $<b_i'^2>$ and cross-correlations $<b_i'b_j'>$ at the points of intersection of the beams. Detailed equations are presented in the Appendix. The so-called realizability conditions can serve as a simple and visual indicator of the the method's adequacy, in particular, the positive definiteness of the diagonal elements of the tensor (intensities of pulsations along the orthogonal axes) and the fulfillment of the Cauchy-Schwarz inequalities $<u_iu_j>^2 \leq <u_i^2> <u_j^2>$ (repeated indices do not sum).

In the first setting (SC), the realizability conditions were satisfied over the entire time interval for the intensities of pulsations along the X and Z axes (fig. 5, *a*, see Inset), even for the minimum averaging period of 100 minutes. Partly, it is due to the design of the experiment that facilitated the calculations of all three components of the Reynolds tensor in the XZ plane. The components can be calculated autonomously using three directly calculated quantities ($b_1'^2>$, $< b_4'^2>$ and $< b_1'b_4'>$) at the point of intersection of beams 1 and 4 (see formula (A2) in the Appendix). The root-mean-square values (r.m.s.) of pulsations along the X and Z axes reached values of 2.5 mm/s and 1.2 mm/s, respectively, and their ratio varied within 1.3–3.0.

The time variation of the convective velocity w^* calculated from the buoyancy flux can be considered a direct indicator of energy pumping. The ratio of the r.m.s. vertical velocity fluctuations to w^* is an important parameter for describing energy redistribution. Its value, obtained in the study of various geophysical currents, varies within a wide range from 0.1 to 0.7 [20]. In this work, an estimate of ~0.3 was obtained for this parameter, and the ratio of w^* and (r.m.s.) of horizontal pulsations turns out to be very close to 1.

The other three components of the tensor are determined with lower accuracy, while at some times, nonphysical (negative) values for the intensity of pulsations along the Y-axis were obtained. However, these intervals, marked by shading in fig. 5, *b*, are small and decrease significantly with an increase in the averaging period. As shown by a comparison of fig. 4 and 5*b*, the local violation of the realizability conditions can be explained by coincidence with the local homogeneity disruption. It should be noted that the total intensity of pulsations in the horizontal plane remained positively definite throughout the entire measurement period.

As for the temporal variability of turbulent stresses, note their daily periodicity, and a significant (~2–3 *h*) delay compared to changes in the radiation flux. The inertia effect, found in both devices, is represented by comparing the curves describing the change in stresses and convective velocity w^*. In [16], a similar delay was found when calculating the energy dissipation rate in the convective layer of an ice-covered lake.

Significant variations in all turbulent stresses during daylight hours should be noted also. In the presence of an average current, such variations can be interpreted as the result of scanning of large, non-uniform, in terms of turbulence parameters, convective cells that are moving past the instrument. Moreover, the time scale of these variations allows the estimation of the horizontal dimensions of such cells. As shown in [15], their sizes can reach tens of meters in large lakes.

In the second setting (DC), when the instruments were twice as close to each other, the condition of local homogeneity was met with acceptable accuracy practically during the entire 6-day measurement period (fig. 6, see Inset). On the other hand, in this setting, the configuration of the beams eliminated a certain “privilege” of the *XZ* plane, and the risk of realizability conditions violation was not associated with any specific components of the tensor. Accordingly, these violations were found for several tensor components, including the intensities of pulsations along the *Y* and *Z* axes (fig. 6).

The corresponding time intervals, however, were significantly reduced with an increase in the averaging period to 150–200 minutes. On the whole, the appearance of “nonphysical” intervals in the DC setting (especially significant for vertical pulsations) can be explained by the instability of the convective structure under conditions of a weak and unstable radiation flux.

The under-ice warming conditions in the DC formulation were more variable, yet, the variability of turbulent stresses demonstrates the same basic features as in the SC formulation: correlation with radiative flux, lag, and variability during daylight hours. The quantitative estimates for the intensity of the pulsations are also consistent with those obtained in the first setting. The only exception is two days with a low level of solar radiation, when the intensities of the pulsations were very small, at the level of the instrument noise.

The stress calculation errors were estimated to verify the results. During the experiment, both devices operated in a high-precision mode (pulse-coherent mode); however, even in this case, the noise level of the initial signal was relatively high. This noise decrease was the main reason for the two-stage averaging procedure. In this case, the preliminary averaging, as noted above, was carried out over a 16-second interval ($n_1 = 32$ pulses with a frequency of 2 Hz; 16 s). The time scale of this averaging was linked to the Kolmogorov dissipative time scale $t_d = (\eta / \varepsilon)^{1/2}$ (η is the kinematic viscosity, ε is the rate of energy dissipation), following that the turbulent pulsations themselves are represented by frequencies with an upper threshold t_d^{-1}. The efficiency of such a procedure for reducing (by a factor of $\sqrt{n_1}$) the instrumental noise was reported in [21]. In our case, this procedure made it possible to reduce the noise level to values below 10^{-3} m/s, following the results obtained earlier in [22] when studying the field of internal waves with weak energy, with similar device settings.

At the second stage, following the methodology presented in [21, 23], the ensemble averaging over time intervals of 50–100 minutes was done (that is, using $n_2 = 50$–100 “instantaneous” velocity values obtained from the results of preliminary averaging). In this case, the errors for the stress $\sigma_{R,i}$ were calculated under the standard assumptions by the formula:

$$\sigma_{R,i}^2 = \frac{2}{n_2} \sum_{j=1}^{6} M_{ij}^{-12} B_j^2 .$$

The calculation results are illustrated in fig. 7 (see Inset), which presents the confidence intervals for all six components of the stress tensor at 95% confidence for the first two days of measurements.

For different components of the Reynolds tensor, the error estimates differ significantly, which was expected, considering the “privilege” of the *XZ* plane noted in the text and the high sensitivity of the calculations to the angular spacing of the beams. In particular, the error in determining the maximum values varies from 10% (for $< u_1'^2 >$ and $< u_3'^2 >$) up to 30–40%. The most problematic for a given instrument configuration is the component $< u_2'^2 >$. Here, even for problematic components, the threshold detected values turned out to be relatively low, reaching 0.3–1.4 mPa.

In addition, note that the results presented should be considered only as an estimate of the error from below. In particular, using the simplest formula, interbeam correlations and temporal autocorrelation of signals for each beam were not taken into account. Refinement of these calculations, and the search for the optimal instrument configurations to reduce the error, is one of the priorities for further work.

5. Discussion

5.1. Beam intensities

The estimates presented in the previous section are based on a quantitative analysis of the experimentally obtained intensities $<b'^2_i>$ of pulsations of the beam velocity components and cross-correlations at the intersection points. All these values are relatively small in the conditions of the under-ice convectively mixed layer. Nevertheless, even in conditions of a weak signal, a significant difference in intensities is recorded for different beams. It is important to emphasize that this difference is not a consequence of significant errors, although the latter, of course, have an impact. The main reasons are the violation of the local horizontal homogeneity and the anisotropy of the stress tensor. The coincidence of the values (within the measurement errors) of the quantities $<b'^2_i>$ can be expected only in the case of isotropic turbulence, which is formally confirmed by the analysis of the matrix connecting these values with the components of the Reynolds tensor (see Appendix). As a consequence, even estimates of the total turbulence energy based on the averaging of beam intensities [1, 7] can be considered only as a very rough approximation as the sum of the three terms $<b'^2_i>$ depends on the anisotropy parameters. Geophysical currents in the overwhelming majority of cases are anisotropic, and, accordingly, the intensities $<b'^2_i>$ do not coincide in magnitude. The analysis of these differences is a feature of the method proposed in this work.

5.2. Energy-containing structures in the CML

The method proposed in this work allows for a comparative analysis of the variability of the averaged and pulsation velocity components, which is essential for elucidating the mechanism of heat transfer in the convective layer. The question of this mechanism's nature and, accordingly, of the spatial structure of the CML remains unanswered. In particular, there is a discussion if the heat transfer is due to the presence of sufficiently stable quasi-deterministic cells, or does it occur through irregular collapses ("thermals", "plumes") under conditions of undeveloped unstable stratification?

The first interpretation is indirectly supported by the results reported in [24], in which the horizontal structure of the CML was investigated with underwater gliders. At the same time, both individual ("chimney") cells, the size of which is comparable to the thickness of the CML, and their comparatively ordered aggregates were found.

The results obtained in this work indicate that the intensities of the pulsation components of the velocity in the CML change with a well-pronounced daily periodicity (fig. 5, 6). At the same time, the averaged horizontal velocity components have no diurnal periodicity, however, there are oscillations of very significant amplitude with a shorter (several hours) period comparable to the relaxation time $\tau \sim h/w^*$ (fig. 4). In this regard, it can be assumed that the nature of the temporal variability of the averaged velocities reflects the structure of the largest and most stable energy-containing vortices (convective cells) [15, 16]. However, why these oscillations practically do not diminish at night, and, accordingly, the structures are preserved for a significant period in the absence of radiation, remains an open question. Possibly, the factor contributing to such survival of structures may be the two-dimensionalization of the mean current at night. To prove this hypothesis, it is necessary to analyze the anisotropic structure of turbulence with the second and third invariants of the Reynolds tensor, which is a work in progress. The analysis of two-dimensional (frequency-depth) spectra of pulsations of various velocity components [25] at night and daytime may also appear to be of use.

5.3. Turbulent diffusion

The calculated values of turbulent stresses can serve as the basis for such an applied problem as a separate assessment of the vertical and horizontal diffusion coefficients K for a convective layer.

The coefficient K is an essential quantitative characteristic of the transport of dissolved substances, in particular, dissolved gases [26]. Horizontal diffusion from coastal sources [27] and vertical transport of methane accumulated in the bottom layers [28] play a significant but quantitatively not fully defined role in the circulation of methane in lakes [28]. The K in a convective layer can be estimated based on the Prandtl representation $K \sim u\, l$, where u and l are the characteristic scales of the velocity and size of the energy-containing pulsations.

The considerable (approximately threefold) difference between the r.m.s. velocity fluctuations in the vertical and horizontal planes obtained in the course of calculations indirectly indicates a significant anisotropy of turbulent transport in the convective layer of ice-covered lakes during spring convection. Taking into account also that the horizontal dimensions of convective cells are several times larger than their vertical scale (see, for example, [29]), it can be concluded that the coefficients of vertical and horizontal diffusion in such a medium may differ by an order of magnitude. In the future, it is planned to concretize these conclusions based on an estimate of the characteristic sizes of pulsations, using the method proposed in [15] for progressive vector diagrams analysis of the velocity components.

6. Conclusion

The paper proposes a method for all components of the turbulent stress tensor calculation using two ADCPs. The method was tested using the data of a field experiment, including measurements of water temperature, current velocities, and under-ice radiation in a convectively mixed layer of a boreal ice-covered lake in spring. Despite the relative weakness of the velocity signal, physically consistent results were obtained on the time variation of the pulsations' intensities and off-diagonal components of the Reynolds tensor. A correlation was found between the turbulence parameters and the radiation flux, which determines the energy pumping. A quantitative assessment of the degree of pulsations' anisotropy is obtained, and the possible causes of its occurrence and daily variability are analyzed. It is shown that the calculation results are very sensitive to the degree of the condition of horizontal flow homogeneity fulfillment.

7. Funding

This work was carried out within the framework of the state assignment of the NWPI KarRC RAS and RFBR grant 18-05-60291, KarRC RAS and RFBR grant 18-05-60291. Research by Kirillin G.B. supported by the German Research Society (DFG grants KI-853–13 / 1, KI-853–16 / 1) and the Sino-German Center for Science Support (CDZ grant GZ1259).

Appendix. Calculation of turbulent stresses from the correlations of the pulsations of the beam velocity components.

The calculation is based on a system of equations connecting the intensities of beam pulsations with the sought elements of the Reynolds tensor:

$$\begin{pmatrix} < b_1'^2 > \\ < b_2'^2 > \\ < b_3'^2 > \\ < b_4'^2 > \\ < b_5'^2 > \\ < b_6'^2 > \end{pmatrix} = \sin^2\alpha_0 \begin{pmatrix} 1 & 0 & 2ctg\alpha_0 & 0 & 0 & ctg^2\alpha_0 \\ 1/4 & -\sqrt{3}/2 & -ctg\alpha_0 & 3/4 & \sqrt{3}ctg\alpha_0 & ctg^2\alpha_0 \\ 1/4 & \sqrt{3}/2 & -ctg\alpha_0 & 3/4 & -\sqrt{3}ctg\alpha_0 & ctg^2\alpha_0 \\ 1 & 0 & -2ctg\alpha_0 & 0 & 0 & ctg^2\alpha_0 \\ 1/4 & -\sqrt{3}/2 & ctg\alpha_0 & 3/4 & -\sqrt{3}ctg\alpha_0 & ctg^2\alpha_0 \\ 1/4 & \sqrt{3}/2 & ctg\alpha_0 & 3/4 & \sqrt{3}ctg\alpha_0 & ctg^2\alpha_0 \end{pmatrix} \begin{pmatrix} < u_x'^2 > \\ < u_x'u_y' > \\ < u_x'u_z' > \\ < u_y'^2 > \\ < u_y'u_z' > \\ < u_z'^2 > \end{pmatrix}.$$

The determinant of the coefficient matrix of this system vanishes, i.e., one of the equations is not independent. A similar problem arises using two 4-beam instruments. In this setting, as shown in [30], this problem can be overcome by the orientation change of one of the devices. In this case, however, the tilt of the axis of one of the devices leads to an increase in errors (due to the small angular spacing of some beams), the need to recalculate the cell numbers for each beam, and also increases the probability of violation of the condition of horizontal homogeneity. In this work, the problem is solved differently. One equation (or two in the DC version) of the type (3) for the intensities of beam pulsations is replaced by equation (5) (or two analogous to it in the DC formulation) for the correlations of the pulsations at the points of beams intersections. For example, in the SC setting, the sixth beam can be excluded from consideration, and the system of equations can be written using directly calculated values ($b_1'^2$, $b_2'^2$, $b_3'^2$, $b_4'^2$, $b_5'^2$, $b_1'b_4'$). Other options are also possible, but in any case, depending on the choice of excluded data, either the size of the horizontal "spot" in which the measurements are taken is reduced, or its symmetry is violated.

There are no fundamental differences between the various options, but in real experimental conditions, when the signal is rather weak, and the assumption of local horizontal homogeneity is fulfilled only in a certain approximation, the choice of an option can significantly affect the accuracy of the results obtained in the calculation.

In this work, to minimize the errors in the calculations, we did not use the beam intensities directly, but their linear combinations corresponding to the symmetry character of the beam configuration. In particular, in the SC formulation, the combinations can be represented as the following six-dimensional "vector" B_i:

$$B_i = \left(b_1'^2, b_4'^2, b_1'b_4', b_2'^2 - b_3'^2, b_5'^2 - b_6'^2, b_2'^2 + b_3'^2 + b_5'^2 + b_6'^2\right).$$

Similarly, we represent the sought components of the Reynolds tensor in the form of "6 — vector": $R_i = \left(< u_x'^2 >, < u_x'u_y' >, < u_x'u_z' >, < u_y'^2 >, < u_y'u_z' >, < u_z'^2 >\right)$. In this case, the system of equations for R_i can be written in the following compact form:

$$B_i = M_{ij}R_j,\ i, j = 1...6, \qquad \text{(A1)}$$

where 6 × 6 matrix M has a form:

$$\mathbf{M}=\sin^2\alpha_0\begin{pmatrix} 1 & 0 & 2ctg\alpha_0 & 0 & 0 & ctg^2\alpha_0 \\ 1 & 0 & -2ctg\alpha_0 & 0 & 0 & ctg^2\alpha_0 \\ -1 & 0 & 0 & 0 & 0 & ctg^2\alpha_0 \\ 0 & \sqrt{3} & 0 & 0 & -2\sqrt{3} & 0 \\ 1/4 & \sqrt{3} & 0 & 0 & 2\sqrt{3} & 0 \\ 1 & 0 & 0 & 3 & 0 & 4ctg^2\alpha_0 \end{pmatrix}. \qquad \text{(A2)}$$

Technically, the solution to system (A1) is reduced to finding the inverse matrix M^{-1}.

Note that in the presented variant of the choice of the system, the first three equations form an autonomous subsystem for the $u_x'^2$, $u_z'^2$, $u_x'\ u_z'$ tensor components. Its solution is as follows:

$$\begin{cases} <u_x'^2>=\left(<b_1'^2>+<b_4'^2>-2<b_1'b_4'>\right)/\,4 \\ <u_z'^2>=\left(<b_1'^2>+<b_4'^2>+2<b_1'b_4'>\right)/\left(4ctg^2\alpha_0\right). \\ <u_x'u_z'>=\left(<b_1'^2>-<b_4'^2>\right)/\,(4ctg\alpha_0) \end{cases}$$

Regarding the DC setting, the results presented in the main text correspond to the following selection of experimental parameters:

$$B_i=\left(b_1'^2+b_4'^2,b_1'^2-b_4'^2,b_2'b_6'+b_3'b_5',b_2'^2+b_6'^2-b_3'^2+b_5'^2,b_3'^2+b_6'^2-b_2'^2-b_5'^2,b_3'^2+b_6'^2+b_2'^2+b_5'^2\right).$$

It should be emphasized that the choice of experimental data for constructing a system of equations is only a technical element of the calculation, and does not fundamentally change its result, although it may improve the estimates.

Литература

1. *Howarth M.J., Souza A.J.* Reynolds stress observations in continental shelf seas // Deep Sea Res II. 2005, 52(9–10). P. 1075–1086.
2. *Guerra M., Thomson J.* Turbulence Measurements from Five-Beam Acoustic Doppler Current Profilers // J. Atmos. Oceanic Technol. 2017. V. 34(6). P. 1267–1284.
3. *Kirillin G.* et al. Turbulence in the stratified boundary layer under ice: observations from Lake Baikal and a new similarity model // Hydrol. Earth Syst. Sci. 2020. V. 24(4). P. 1691–1708.
4. *Lohrmann A., Hackett B., Roed L.* High-resolution measurements of turbulence, velocity, and stress using a pulse-to-pulse coherent sonar // J. Atmos. Oceanic Technol. 1990. V. 7(1). P. 19–37.
5. *Lorke A., Wüest A.* Application of Coherent ADCP for Turbulence Measurements in the Bottom Boundary Layer // J. Atmos. Oceanic Technol. 2005. V. 22. P. 1821–1828.
6. *Wiles P.J.* et al. A novel technique for measuring the rate of turbulent dissipation in the marine environment // Geophys. Res. Lett. 2006. V. 33. L21608. doi: 10.1029/2006GL027050
7. *Nystrom E.A., Rehmann C.R., Oberg K.A.* Evaluation of mean velocity and turbulence measurements with ADCPs // J. Hydraul. Eng. 2007. V. 133(12). P. 1310–1318.
8. *Kirincich A.R., Rosman J.H.* A Comparison of methods for estimating reynolds stress from ADCP measurements in wavy environments // J. Atmos. Oceanic Technol. 2011. V. 28. P. 1539–1553. doi: 10.1175/JTECH-D-11–00001.1
9. *Farmer D.M.* Penetrative convection in the absence of mean shear // QJR Meteorol. Soc. 1975. V. 101. P. 869–891. doi: 10.1002/qj.49710143011
10. *Mironov D.* et al. Radiatively driven convection in ice-covered lakes: Observations, scaling, and a mixed layer model // J. Geophys. Res. 2002. V. 107(C4). doi: 10.1029/2001JC000892
11. *Petrov M.P.* et al. Motion of water in an ice-covered shallow lake // Water Resources. 2007. V. 34(2). P. 113–122.
12. *Kirillin G.* et al. Physics of seasonally ice-covered lakes: a review // Aquat Sci. 2012. V. 74. P. 659–682. doi: 10.1007/s00027–012–0279-y
13. *Bouffard D.* et al. Ice-covered Lake Onega: effects of radiation on convection and internal waves // Hydrobiologia. 2016. V. 780 (1). P. 21–36. doi: 10.1007/s10750–016–2915–3
14. *Kirillin G.* et al. Turbulent mixing and heat fluxes under lake ice: the role of seiche oscillations // Hydrol. Earth Syst. Sci. 2018. V. 22. P. 6493–6504. doi: 10.5194/hess-22–6493–2018
15. *Bogdanov S.* et al. Structure and dynamics of convective mixing in Lake Onego under ice-covered conditions // Inland Waters. 2019. V. 9(2). P. 177–192. doi: 10.1080/20442041.2018.1551655

16. *Volkov S.* et al. Fine scale structure of convective mixed layer in ice-covered lake // Environ. Fluid Mech. 2019. V. 19. P. 751–764. doi: 10.1007/s10652–018–9652–2
17. *Zdorovennov R.* et al. Interannual variability of ice and snow cover of a small shallow lake // Est. J. Earth Sci. 2013. V. 61(1). P. 26–32. doi: 10.3176/earth.2013.03
18. *Greene A.D.* et al. Using an ADCP to estimate turbulent kinetic energy dissipation rate in sheltered coastal waters // J. Atmos. Oceanic Technol. 2015. V. 32. P. 318–333.
19. *Deardorff J.W.* Preliminary results from numerical integrations of the unstable planetary boundary layer // J. Atmos. Sci. 1970. V. 27. P. 1209–1211.
20. *MacIntyre S.* et al. Turbulence in a small Arctic pond // Limnol. Oceanogr. 2018. V. 63(6). P. 2337–2358. doi: 10.1002/lno.10941
21. *Williams E., Simpson J.H.* Uncertainties in estimates of reynolds stress and TKE production rate using the ADCP variance method // J. Atmos. Oceanic Technol. 2004. V. 21. P. 347–357. doi: 10.1175/1520–0426(2004)021<0347: UIEORS>2.0.CO;2
22. *Henderson S.M.* Turbulent production in an internal wave bottom boundary layer maintained by a vertically propagating seiche // J. Geophys. Res. Oceans. 2016. V. 121, N4. P. 2481–2498. doi: 10.1002/2015JC011071
23. *Stacey M.T.*, *Monismith S.G.*, *Burau J.R.* Measurements of Reynolds stress profiles in unstratified tidal flow // J. Geophys. Res. 1999. V. 104(C5). P. 10933–10949. doi: 10.1029/1998JC900095
24. *Forrest A.L.* et al. Convectively driven transport in temperate lakes // Limnol. Oceanogr. 2008. V. 53(5). P. 2321–2332. doi: 10.4319/lo.2008.53.5_part_2.2321
25. *Korotenko K.A., Sentchev A.V., Schmitt F.G.* Effect of variable winds on current structure and Reynolds stresses in a tidal flow: Analysis of experimental data in the eastern English Channel // Ocean Sci. 2012. V. 8(6). P. 1025–1040. doi: 10.5194/os-8–1025–2012
26. *Yang B., Wells M., Li J., Yang J.* Mixing, stratification and plankton under lake-ice during winter in a large lake: implications for spring dissolved oxygen levels // EarthArXiv Preprimts. 2019. Preprint. doi: 10.31223/osf.io/5uvwc
27. *DelSontro T., del Giorgio P.A., Prairie Y.T.* No longer a paradox: the interaction between physical transport and biological processes explains the spatial distribution of surface water methane within and across lakes // Ecosystems. 2018. V. 21(6). P. 1073–1087.
28. *McGinnis D.F.* et al. Enhancing surface methane fluxes from an oligotrophic lake: exploring the microbubble hypothesis // Environ. Sci. Technol. 2015. V. 49(2). P. 873–880.
29. *Austin J.A.* Observations of radiatively driven convection in a deep lake // Limnol. Oceanogr. 2019. V. 64(5). P. 2152–2160. doi: 10.1002/lno.11175
30. *Vermeulen B.*, *Hoitink A.J.F.*, *Sassi M.G.* Coupled ADCPs can yield complete Reynolds stress tensor profiles in geophysical surface flows // Geophys. Res. Lett. 2011. V. 38. L06406. doi: 10.1029/2011GL046684

References

1. *Howarth M.J.*, *Souza A.J. Reynolds stress observations in continental shelf seas. Deep Sea Res II*. 2005, 52(9–10), 1075–1086.
2. *Guerra M.*, *Thomson J.* Turbulence measurements from five-beam acoustic doppler current profilers. *J. Atmos. Oceanic Technol.* 2017, 34(6), 1267–1284.
3. *Kirillin G.* et al. Turbulence in the stratified boundary layer under ice: observations from Lake Baikal and a new similarity model. *Hydrol. Earth Syst. Sci.* 2020, 24(4), 1691–1708.
4. *Lohrmann A.*, *Hackett B.*, *Roed L.* High-resolution measurements of turbulence, velocity, and stress using a pulse-to-pulse coherent sonar. *J. Atmos. Oceanic Technol.* 1990, **7**(1), 19–37.
5. *Lorke A.*, *Wüest A.* Application of coherent ADCP for turbulence measurements in the bottom boundary layer. *J. Atmos. Oceanic Technol.* 2005, 22, 1821–1828.
6. *Wiles P.J.* et al. A novel technique for measuring the rate of turbulent dissipation in the marine environment. *Geophys. Res. Lett.* 2006, 33, L21608. doi: 10.1029/2006GL027050
7. *Nystrom E.A.*, *Rehmann C.R.*, *Oberg K.A.* Evaluation of mean velocity and turbulence measurements with ADCPs. *J. Hydraul. Eng.* 2007, 133(12), 1310–1318.
8. *Kirincich A.R., Rosman J.H.* A Comparison of Methods for Estimating Reynolds Stress from ADCP Measurements in Wavy Environments. *J. Atmos. Oceanic Technol.* 2011, 28, 1539–1553. doi: 10.1175/JTECH-D-11–00001.1
9. *Farmer D.M.* Penetrative convection in the absence of mean shear. *QJR Meteorol. Soc.* 1975, 101, 869–891. doi: 10.1002/qj.49710143011
10. *Mironov D.* et al. Radiatively driven convection in ice-covered lakes: Observations, scaling, and a mixed layer model. *J. Geophys. Res.* 2002, 107(C4). doi: 10.1029/2001JC000892

11. *Petrov M.P.* et al. Motion of Water in an Ice-Covered Shallow Lake. *Water Resources*. 2007, 34(2), 113–122.
12. *Kirillin G.* et al. Physics of seasonally ice-covered lakes: a review. *Aquat Sci.* 2012, 74, 659–682. doi: 10.1007/s00027–012–0279-y
13. *Bouffard D.* et al. Ice-covered Lake Onega: effects of radiation on convection and internal waves. *Hydrobiologia*. 2016, 780 (1), 21–36. doi:10.1007/s10750–016–2915–3
14. *Kirillin G.* et al. Turbulent mixing and heat fluxes under lake ice: the role of seiche oscillations. *Hydrol. Earth Syst. Sci*. 2018, 22, 6493–6504. doi: 10.5194/hess-22–6493–2018
15. *Bogdanov S.* et al. Structure and dynamics of convective mixing in Lake Onego under ice-covered conditions. *Inland Waters*. 2019, 9(2), 177–192.
16. *Volkov S.* et al. Fine scale structure of convective mixed layer in ice-covered lake. *Environ. Fluid Mech*. 2019, 19, 751–764. doi: 10.1007/s10652–018–9652–2
17. *Zdorovennov R.* et al. Interannual variability of ice and snow cover of a small shallow lake. *Est. J. Earth Sci*. 2013, 61(1), 26–32. doi: 10.3176/earth.2013.03
18. *Greene A.D.* et al. Using an ADCP to Estimate Turbulent Kinetic Energy Dissipation Rate in Sheltered Coastal Waters. *J. Atmos. Oceanic Technol*. 2015, 32, 318–333.
19. *Deardorff J.W.* Preliminary results from numerical integrations of the unstable planetary boundary layer. *J. Atmos. Sci*. 1970, 27, 1209–1211.
20. *MacIntyre S.* et al. Turbulence in a small Arctic pond. *Limnol. Oceanogr*. 2018, 63(6), 2337–2358. doi: 10.1002/lno.10941
21. *Williams E.*, *Simpson J.H.* Uncertainties in Estimates of Reynolds Stress and TKE Production Rate Using the ADCP Variance Method. *J. Atmos. Oceanic Technol.* 2004, 21, 347–357. doi: 10.1175/1520–0426(2004)021<0347: UIEORS>2.0.CO;2
22. *Henderson S.M.* Turbulent production in an internal wave bottom boundary layer maintained by a vertically propagating seiche. *J. Geophys. Res. Oceans*. 2016, 121. doi: 10.1002/2015JC011071
23. *Stacey M.T.*, *Monismith S.G.*, *Burau J.R.* Measurements of Reynolds stress profiles in unstratified tidal flow. *J. Geophys. Res*. 1999*,* 104(C5), 10933–10949, doi: 10.1029/1998JC900095
24. *Forrest A.L.* et al. Convectively driven transport in temperate lakes. *Limnol. Oceanogr*. 2008, 53(5), 2321–2332. doi: 10.4319/lo.2008.53.5_part_2.2321
25. *Korotenko K.A.*, *Sentchev A.V.*, *Schmitt F.G.* Effect of variable winds on current structure and Reynolds stresses in a tidal flow: Analysis of experimental data in the eastern English Channel. *Ocean Sci.* 2012, 8(6), 1025–1040. doi: 10.5194/os-8–1025–2012
26. *Yang B.*, *Wells M.*, *Li J.*, *Yang J.* Mixing, stratification and plankton under lake-ice during winter in a large lake: implications for spring dissolved oxygen levels. *EarthArXiv Preprimts*. 2019, Preprint. doi: 10.31223/osf.io/5uvwc
27. *DelSontro T.*, *del Giorgio P.A.*, *Prairie Y.T.* No longer a paradox: the interaction between physical transport and biological processes explains the spatial distribution of surface water methane within and across lakes. *Ecosystems*. 2018, 21(6), 1073–1087.
28. *McGinnis D.F.* et al. Enhancing surface methane fluxes from an oligotrophic lake: exploring the microbubble hypothesis. *Environ. Sci. Technol.* 2015, 49(2), 873–880.
29. *Austin J.A.* Observations of radiatively driven convection in a deep lake. *Limnol. Oceanogr*. 2019, 64(5), 2152–2160. doi:10.1002/lno.11175
30. *Vermeulen B.*, *Hoitink A.J.F.*, *Sassi M.G.* Coupled ADCPs can yield complete Reynolds stress tensor profiles in geophysical surface flows. *Geophys. Res. Lett*. 2011, 38, L06406. doi: 10.1029/2011GL046684

К статье *Богданов С.Р.*, *Здоровеннов Р.Э.*, *Пальшин Н.И.*, *Здоровеннова Г.Э.*, *Тержевик А.Ю.*, *Гавриленко Г.Г.*, *Волков С.Ю.*, *Ефремова Т.В.*, *Кулдин Н.А.*, *Кириллин Г.Б.* Расчет турбулентных напряжений в конвективно-перемешанном слое в мелководном озере подо льдом...

Bogdanov S.R., *Zdorovennov R.E.*, *Palshin N.I.*, *Zdorovennova G.E.*, *Terzhevik A.Yu.*, *Gavrilenko G.G.*, *Volkov S.Yu.*, *Efremova T.V.*, *Kuldin N.A.*, *Kirillin G.B.* Deriving of turbulent stresses in a convectively mixed layer in a shallow lake under ice...

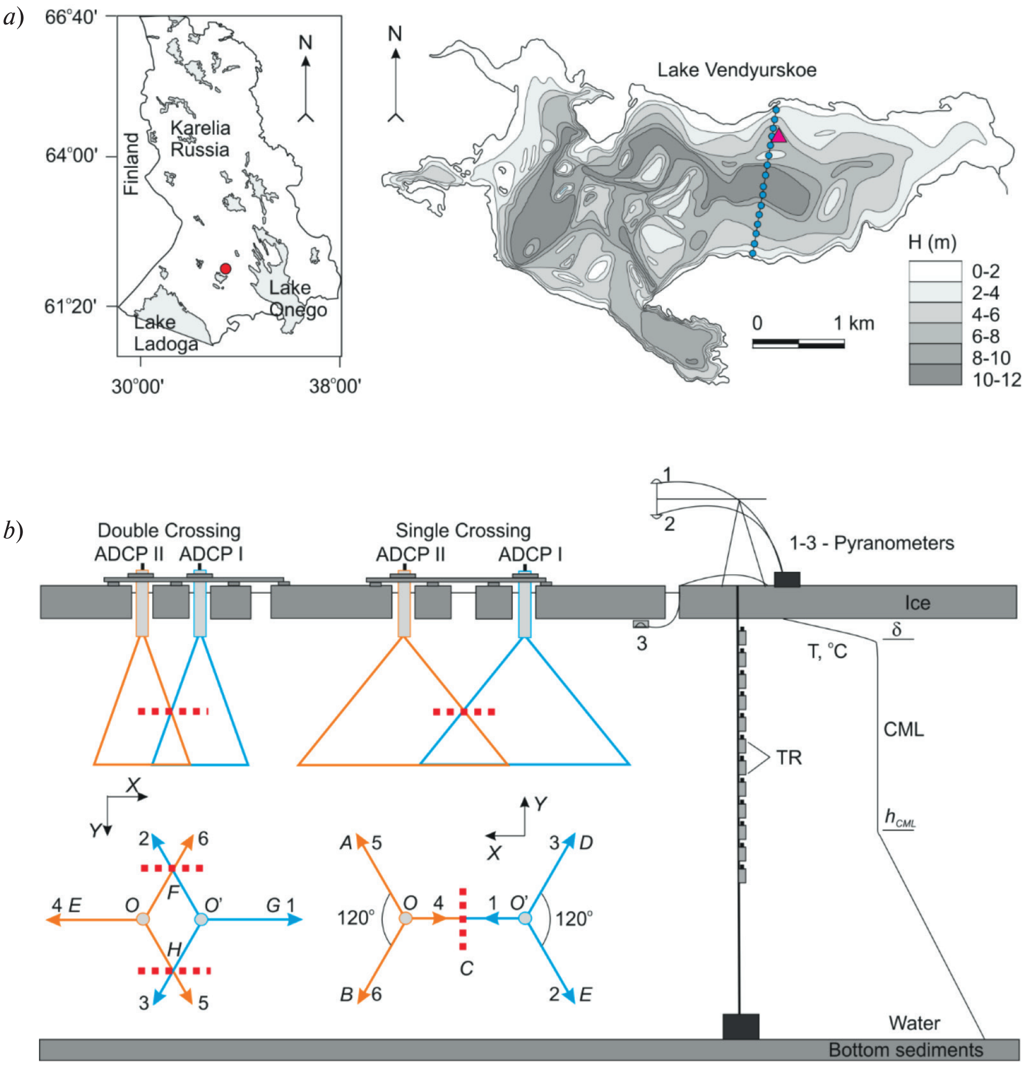

Fig. 1. *a* — Location and bathymetry of the Lake Vendyurskoe (red dot) with indication of the measuring complex (red triangle) and measuring stations (blue circles). *b* — Scheme of the measuring complex. Indexes 1, 2, 3 — the beams of the first device, 4, 5, 6 — the second; in this case beams 1 and 4 lie in the *XZ* plane. *O* and *O* ‘ — emitters of devices.

К статье *Богданов С.Р.*, *Здоровеннов Р.Э.*, *Пальшин Н.И.*, *Здоровеннова Г.Э.*, *Тержевик А.Ю.*, *Гавриленко Г.Г.*, *Волков С.Ю.*, *Ефремова Т.В.*, *Кулдин Н.А.*, *Кириллин Г.Б.* Расчет турбулентных напряжений в конвективно-перемешанном слое в мелководном озере подо льдом...

Bogdanov S.R., *Zdorovennov R.E.*, *Palshin N.I.*, *Zdorovennova G.E.*, *Terzhevik A.Yu.*, *Gavrilenko G.G.*, *Volkov S.Yu.*, *Efremova T.V.*, *Kuldin N.A.*, *Kirillin G.B.* Deriving of turbulent stresses in a convectively mixed layer in a shallow lake under ice...

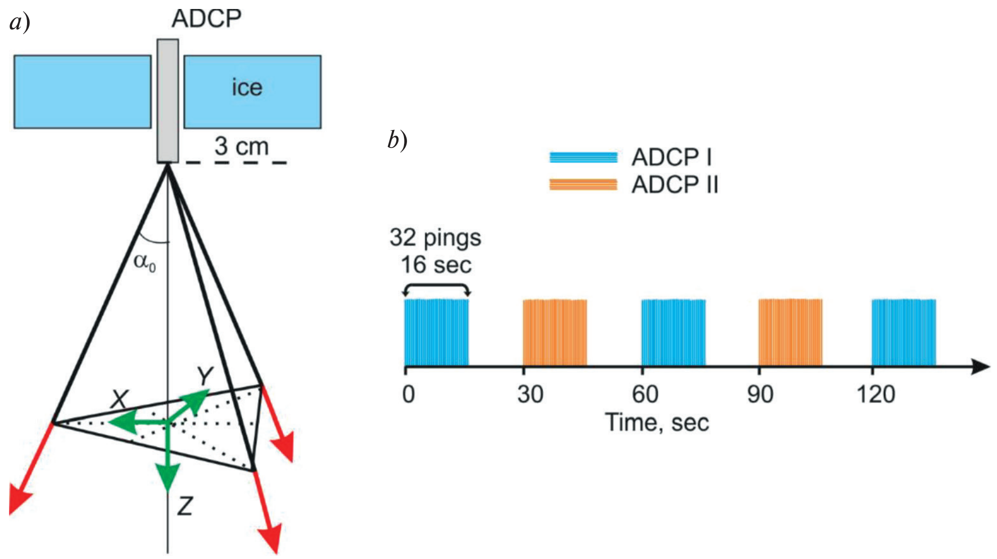

Fig. 2. *a* — ADCP Ice Installation, *b* — Pulse train for asynchronous operation of two ADCPs.

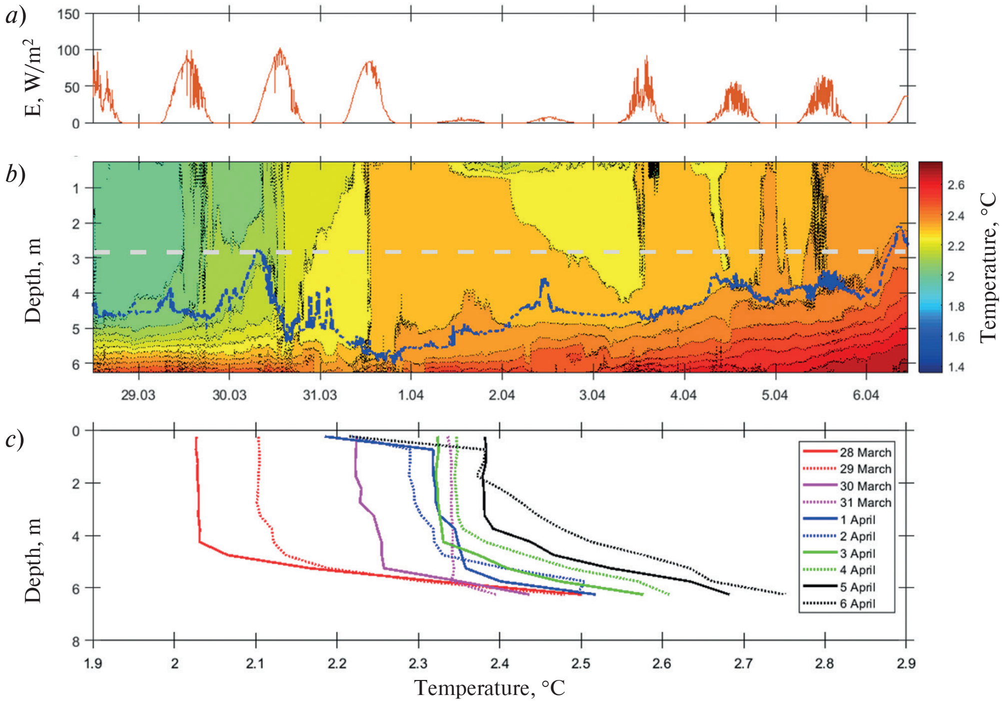

Fig. 3. Fluxes of solar radiation at the lower boundary of ice (*a*) and temperature of the water column (*b*) March 28—April 6, 2020. *c* — vertical temperature profiles. The blue line on the panel (*b*) is the lower boundary of the CML, the gray dotted line is the ADCP scan area.

К статье *Богданов С.Р.*, *Здоровеннов Р.Э.*, *Пальшин Н.И.*, *Здоровеннова Г.Э.*, *Тержевик А.Ю.*, *Гавриленко Г.Г.*, *Волков С.Ю.*, *Ефремова Т.В.*, *Кулдин Н.А.*, *Кириллин Г.Б.* Расчет турбулентных напряжений в конвективно-перемешанном слое в мелководном озере подо льдом...

Bogdanov S.R., *Zdorovennov R.E.*, *Palshin N.I.*, *Zdorovennova G.E.*, *Terzhevik A.Yu.*, *Gavrilenko G.G.*, *Volkov S.Yu.*, *Efremova T.V.*, *Kuldin N.A.*, *Kirillin G.B.* Deriving of turbulent stresses in a convectively mixed layer in a shallow lake under ice...

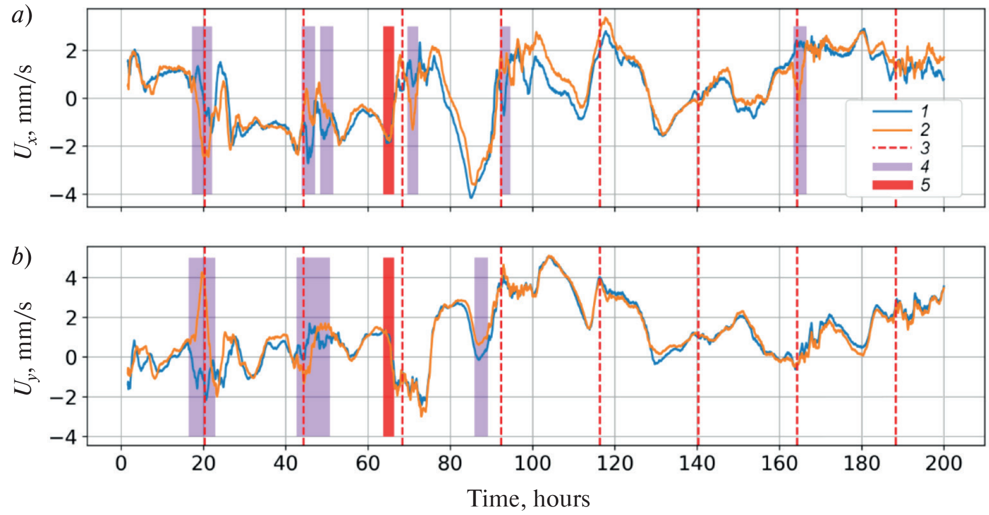

Fig. 4. The dependance of the horizontal components of the average velocity U_x (*a*) and U_y (*b*) on time, calculated from data of two ADCPs at a depth of 1.61 m. The zero of the horizontal axis corresponds to the start of the measurements (16:30 03.27.2020). *1* — I ADCP, *2* — II ADCP, *3* — noon, *4* — time intervals when the homogeneity condition was disrupted, *5* — change of settings.

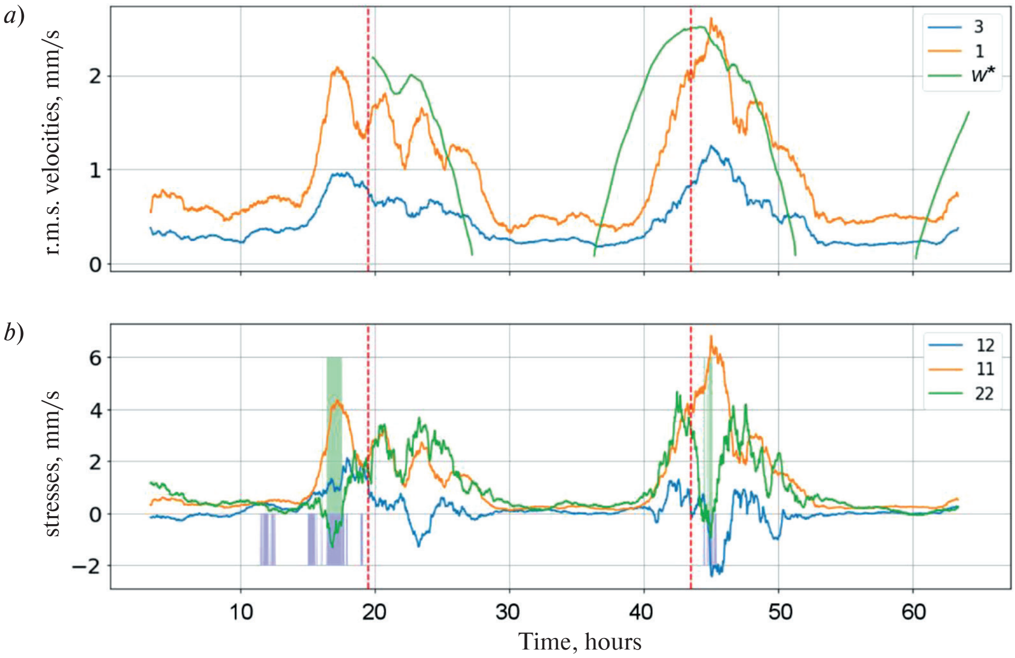

Fig. 5. *a* — The dependence of convective velocity w^* and of the intensities of turbulent pulsations along the axes *X* (1), *Z* (3) on time. Setting SC. *b* — Turbulent stresses in the XY plane, setting SC. Pairs of numbers indicate the indices of the corresponding elements of the Reynolds tensor. Here and in fig. 6 the shaded areas in the region of negative and positive ordinates serve as indicators of time intervals when, respectively, the Cauchy-Schwarz condition $\langle u_1u_2\rangle^2 \le \langle u_1^2\rangle \langle u_2^2\rangle$ and the positive definiteness of the pulsation intensities were violated.

К статье *Богданов С.Р., Здоровеннов Р.Э., Пальшин Н.И., Здоровеннова Г.Э., Тержевик А.Ю., Гавриленко Г.Г., Волков С.Ю., Ефремова Т.В., Кулдин Н.А., Кириллин Г.Б.* Расчет турбулентных напряжений в конвективно-перемешанном слое в мелководном озере подо льдом...

Bogdanov S.R., Zdorovennov R.E., Palshin N.I., Zdorovennova G.E., Terzhevik A.Yu., Gavrilenko G.G., Volkov S.Yu., Efremova T.V., Kuldin N.A., Kirillin G.B. Deriving of turbulent stresses in a convectively mixed layer in a shallow lake under ice...

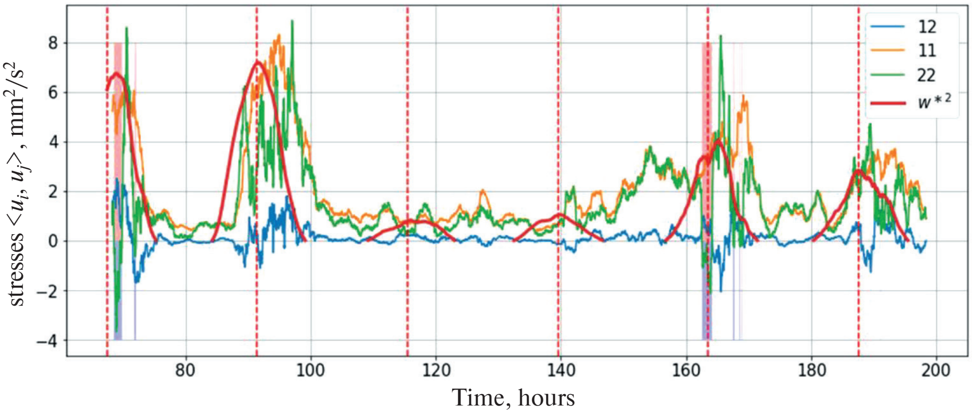

Fig. 6. The dependence of turbulent stresses in the *XY* plane (12, 11, 22) and the square of the convective velocity (w^{*2}) on time.

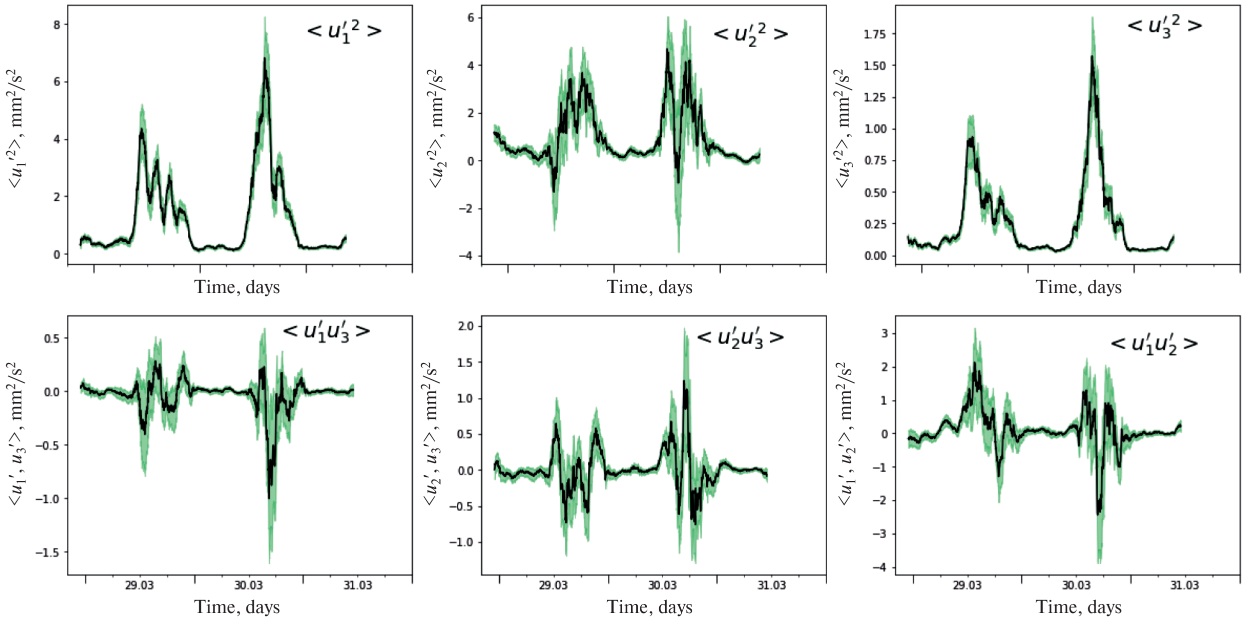

Fig. 7. Results of stresses calculations for the confidence probability 95%.